Electronic and optical properties of $PbTe/Pb_{1-x}Eu_xTe$ multiple-quantum-well structures

Shu Yuan, G. Springholz, and G. Bauer
Institut für Halbleiterphysik, Universität Linz, A-4040 Linz, Austria

M. Kriechbaum
Institut für Theoretische Physik, Universität Graz, A-8010 Graz, Austria

(Received 7 October 1993)

The frequency dependence of the absorption constant $\alpha(\omega)$ and the enhancement of the refractive index $n(\omega)$ in the region of interband transitions between confined quasi-two-dimensional states of the valence and conduction bands of $PbTe/Pb_{1-x}Eu_xTe$ multiple-quantum well (MQW) structures is studied experimentally as well as theoretically. Transmission, reflectivity, and photoconductivity spectra of several MQW's with PbTe well widths from 62 to 118 Å and $Pb_{1-x}Eu_xTe$ barrier widths from 486 to 621 Å ($x \approx 3\%$) are compared with calculated spectra. The experimental data are compared to calculations of the transmission and reflectivity of the multilayer structures based on frequency-dependent dielectric functions $\epsilon(\omega)$ of the buffer and MQW layers. For the buffer layer experimentally determined values for $\epsilon(\omega)$ are used, whereas for the MQW system the sum of a background dielectric function and an additional term, which takes into account the electronic contribution due to interband transitions between electric subbands in the valence band (VB) and conduction band (CB), are used. For calculating the second term two approaches were followed. The conventional approach is based on treating these interband transitions as originating from confined states within the PbTe wells only. The second, more realistic, approach is based on a complete calculation of the band structure of the MQW systems using a $\mathbf{k}\cdot\mathbf{p}$ envelope function approximation which yields proper energy eigenstates, eigenfunctions, and oscillator strengths. The absorption constant $\alpha(\omega)$ is then obtained from an integration in $\mathbf{k}$ space. The electronic contribution $\delta\epsilon^{\text{VB-CB}}(\omega)$ to the total dielectric function is independent of the position z along the growth direction in the MQW structure, i.e., in this respect the MQW is treated as being optically homogeneous. The calculated transmission and reflectivity data fit the experimental data very well. The steplike changes in $\alpha(\omega)$ result in cusplike changes of the refractive index $n(\omega)$. From a comparison of the experimentally determined interband transition energies with the calculated values on several samples, the conduction-band offset is determined to be $\Delta E_c/\Delta E_g = 0.55 \pm 0.2$.

I. INTRODUCTION

$PbTe/Pb_{1-x}Eu_xTe$ heterostructures are of interest for the fabrication of tunable diode lasers in the midinfrared range (3–6.5 μm).[1] Recently, Feit *et al.*[2] reported the highest cw operating temperature (203 K) for such midinfrared lasers using a buried heterostructure concept. Previously, Partin[1] had achieved up to 175-K cw operation using a side optical cavity quantum-well (QW) structure. The band offsets in these many valley semiconductor materials, with minimum direct gaps at the L points of the Brillouin zone (BZ), have been studied by various methods, including emission wavelengths of laser radiation, photoluminescence, optical absorption measurements, and cyclotron resonance experiments. All reports published so far agree that $PbTe/Pb_{1-x}Eu_xTe$ forms a type-I band alignment in the range of compositions x smaller than 10%. Partin[1] has used $Pb_{1-x}Eu_xSe_yTe_{1-y}$/PbTe QW's where Se had been added to counterbalance the increase of the lattice constant due to europium and thus to achieve lattice-matched QW's. Optical absorption measurements were made on $PbTe/Pb_{1-x}Eu_xTe$ lattice mismatched multiple-quantum wells (MQW's).[3] In QW's with Eu content less than about 5%, the band offsets deduced from the laser emission photon energies and the optical absorption measurements indicated that the conduction-band (CB) and valence-band (VB) discontinuities ($\Delta E_c, \Delta E_v$) are approximately equal.[1–3] However, photoluminescence studies on these QW's with PbTe well widths of the order of 50–90 Å were interpreted as giving evidence for $\Delta E_c/\Delta E_g$ being either 0.1 or 0.9,[4,5] where ΔE_g is the difference of the band gaps. Similar results were obtained from cyclotron resonance experiments[6] on $Pb_{1-x}Eu_xSe_yTe_{1-y}$/PbTe QW's where an offset of $\Delta E_c/\Delta E_g = 0.1$ was deduced. However, $\Delta E_c/\Delta E_g = 0.55$ gave a nearly as good fit. Up to an Eu content of about 5% the energy band gap of the ternary (or quarternary) compound increases rapidly and linearly[1] and consequently the offset should increase linearly as well.

In this paper we present a systematic study on the electronic and optical properties of $PbTe/Pb_{1-x}Eu_xTe$ MQW's with PbTe well widths from 62 to 118 Å and Eu contents x from 2.4% to 3%. The paper is organized as follows. In Sec. II, the molecular-beam epitaxial (MBE) growth of the MQW samples is described as well as the structural characterization using x-ray diffraction and the experimental investigation of their electronic and optical properties. In Sec. III, a simple expression of the absorption coefficient $\alpha(\omega)$ for QW's and the method to obtain

the refractive index $n(\omega)$ from the Kramers-Kronig transformation of $\alpha(\omega)$ is described. The transition energies are determined from fits to the experimental transmission spectra. In Sec. IV, the theoretical approach is presented. The band structure of the MQW's is treated with the standard four band $\mathbf{k}\cdot\mathbf{p}$ Hamiltonian for the lead salt compounds using the envelope function approximation (EFA) for perfectly periodic systems.[7] The input parameters are the band parameters of bulk PbTe and $Pb_{1-x}Eu_xTe$. The EFA theory is used to calculate the superlattice states at the center of the superlattice BZ as a function of the band offset. The band offsets are derived from the quantitative comparison of experimentally observed transition energies in all samples with the calculated ones. In addition, this theory is employed to calculate the dispersion and wave functions throughout the superlattice BZ for a fixed band offset. In Sec. V, the optical properties of these MQW's are calculated in the region of the fundamental absorption edge. The fundamental absorption coefficients $\alpha(\omega)$ are calculated for various interband transitions involving the subband ladders of both the longitudinal as well as the oblique valleys. The calculations are based on two models. One treats the $PbTe/Pb_{1-x}Eu_xTe$ MQW structure as dielectrically homogeneous with respect to the electronic contributions of interband transitions between electric subbands. The other model treats the MQW as a dielectrically nonhomogeneous material, where these interband transitions take place in the QW layers only. The resulting transmission and reflectivity spectra are compared with the experimental spectra. We discuss the model dependence of optical properties of the samples in Sec. VI.

It is shown that both the absorption coefficients and the refractive indices of the $PbTe/Pb_{1-x}Eu_xTe$ MQW's depend on Eu concentration and well and barrier widths. In bulk materials, it is well known that the refractive index exhibits remarkable changes at the fundamental absorption edge. This was investigated by Stern[8] for III-V compounds, by Zemel, Jensen, and Schoolar[9] and Yuan *et al.*[10] for the narrow-gap lead salts, where the band nonparabolicity affects absorption and consequently the refractive index $n(\omega)$. For GaAs/AlAs quantum wells the enhancement of $n(\omega)$ close to interband resonances depends on the well and barrier thicknesses and barrier composition.[11–13] Furthermore electric fields influence the refractive index of QW's, which is important for electrooptic device applications.[14,15]

The dependence of the refractive index $n(\omega)$ of PbTe QW's on the frequency exhibits pronounced maxima close to the interband transitions between confined hole and electron states in $PbTe/Pb_{1-x}Eu_xTe$ multiple-quantum-well structures. In contrast to GaAs/GaAlAs MQW's, excitonic contributions to $n(\omega)$ are practically absent in the lead salt compounds because of their huge dielectric constant.[10]

II. SAMPLES AND MIDINFRARED SPECTROSCOPY

A. Molecular-beam epitaxy of $PbTe/Pb_{1-x}Eu_xTe$ Te MQW's

The MBE growth was carried out in a RIBER MBE growth chamber and custom built preparation and load lock chambers with a background pressure of 5×10^{-10} mbar during growth. For the PbTe growth an effusion cell filled with the PbTe compound is used and an additional Te_2 effusion cell for adjustment of the beam flux composition and the carrier concentration. With such fine adjusted beam flux composition we have recently demonstrated the MBE growth of very high mobility PbTe epilayers with Hall mobilities up to 1.98×10^6 cm^2/Vs, and carrier concentrations in the range of 1×10^{17} cm^{-3} at 5 K.[16] For the growth of $Pb_{1-x}Eu_xTe$ an Eu effusion cell is used in addition to adjust the x composition of the ternary compound and a second Te_2 effusion cell to supply the excess flux of the group-VI (Te) element.[17] The different beam flux rates were determined with an ion gauge beam flux monitor calibrated with a quartz crystal thickness monitor for absolute flux rate measurements.

All films were grown on freshly cleaved BaF_2 (111) substrates at substrate temperatures of 350 °C, which was calibrated with the melting points of different metals.[17] Prior to the MQW growth a comparatively thick $Pb_{1-x}Eu_xTe$ buffer layer of $d=3-5$ μm was deposited on the BaF_2 substrate with an x content identical to that of the $Pb_{1-x}Eu_xTe$ barriers in the subsequent MQW stack. Therefore the $Pb_{1-x}Eu_xTe$ buffer layer is transparent in the spectral range of interest and the x content of the $Pb_{1-x}Eu_xTe$ layers could be determined directly from the absorption edge of the buffer layer. The thickness of the buffer layers was chosen to be large enough to ensure a nearly complete strain relaxation in spite of the high lattice mismatch of 4.2% of the epilayer with respect to the BaF_2 substrates. The structural perfection of the buffer layers was checked by x-ray diffraction rocking curves and typically a width full width at half maximum of about 30 arcsec for PbTe and of 80 arcsec for $Pb_{0.97}Eu_{0.03}Te$ was found. *In situ* reflection high-energy electron diffraction (RHEED) at 35 keV was used to monitor the growth process. For low substrate temperatures we have observed a large number of RHEED intensity oscillations for PbTe and $Pb_{1-x}Eu_xTe$ growth,[17]

TABLE I. Sample parameters of $PbTe/Pb_{1-x}Eu_xTe$ MQW's.

Sample	x (%)	$Pb_{1-x}Eu_xTe$ buffer (μm)	PbTe well (Å)	$Pb_{1-x}Eu_xTe$ barrier (Å)	Number of periods
A	2.6	5.25	62	621	46
B	3.0	3.35	93	554	20
C	2.4	4.62	118	486	30

which can also be used to determine absolute growth rates set in all cases to be close to 1 μm/h. For PbTe growth an additional Te_2 flux of about 8×10^{12} molecule/cm^2 sec and for $Pb_{1-x}Eu_xTe$ growth a Te_2 to Eu flux rate ratio of 2.5 was used.

A series of several PbTe/$Pb_{1-x}Eu_xTe$ MQW samples was grown with well widths between 62 and 118 Å and relatively thick barrier widths of 486–621 Å in order to avoid coupling and miniband formation between the quantum wells. The Eu content in the samples was kept roughly around 3%, which gives a difference of the band gap of the $Pb_{1-x}Eu_xTe$ barriers to the PbTe wells of about 180 meV. For the MQW's on top of the $Pb_{1-x}Eu_xTe$ buffers, the growth was interrupted for 5 sec after completion of each single layer keeping the surface under Te_2 flux in order to promote smoothening of the surface and to improve the interface quality. Despite the strain due to the lattice mismatch between the PbTE and the $Pb_{1-x}Eu_xTe$ layers, the RHEED pattern remained totally streaked during the entire MQW growth process, indicating the persistence of a smooth surface throughout the whole growth sequence.

In the following, experimental investigations on three different MQW samples (*A*,*B*, and *C*; see Table I) are described. In order to determine the exact MQW periods and the thicknesses of the PbTe quantum wells, which are of crucial importance for the determination of the band offsets (see below), all samples were investigated by high-resolution x-ray diffraction techniques using $CuK_{\alpha1}$ radiation. Both standard θ-2θ scans as well as high resolution triple axis scans were performed using a channel cut two-reflection Ge(220) analyzer crystal in the secondary beam. As an example, in Fig. 1, the triple axis x-ray diffraction curve of the (222) Bragg reflection for MQW sample *A* is shown together with a fit based on a dynamical simulation (dashed line). The structural parameters of the sample are given in the inset. We observe sharp superlattice satellite reflection peaks up to the order 8, with only a small increase of the peak broadening with increasing satellite order, which indicates a low degree of interface roughness.

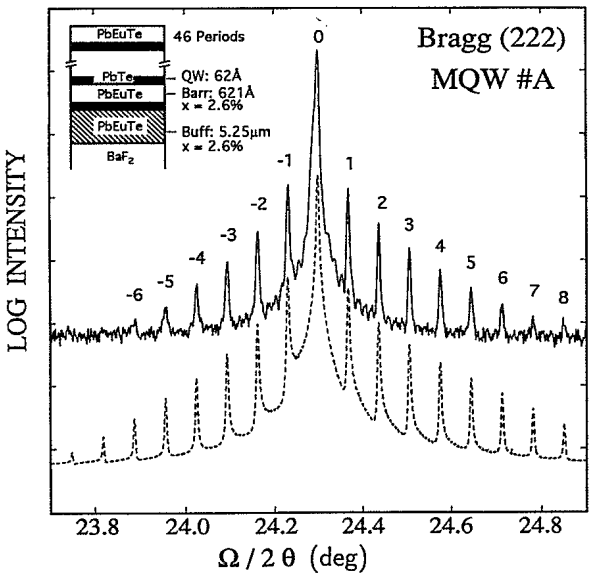

FIG. 1. High-resolution $\Omega/2\Theta$ x-ray diffraction pattern of MQW sample *A*, (222) Bragg reflection, Cu $K\alpha1$ radiation; experimental data (solid line) and calculated diffractogram (dashed line) are based on a simulation using dynamical diffraction theory.

The main peak (*SLO*) in the diffraction trace is the zeroth-order (222) reflection of the whole MQW stack of the sample, whereas the (222) Bragg peak of the $Pb_{1-x}Eu_xTe$ buffer layer is observed just as a weak shoulder on the left-hand side of the main SLO peak. The lattice mismatch between the PbTe QW and the $Pb_{1-x}Eu_xTe$ barriers is only 0.19% for the small x contents of 3% ($a_{PbTe}=6.462$ Å, $a_{Pb_{0.97}Eu_{0.03}Te}=6.47$ Å). Therefore the average lattice constant of the entire MQW stack (with contributions of the thick $Pb_{1-x}Eu_xTe$ barriers and the thin PbTe wells) is almost identical to the lattice constant of the $Pb_{1-x}Eu_xTe$ buffer layer. This results only in a minor shift of the SLO peak with respect to the reflection of the buffer layer. The total thickness of the MQW stack (46 periods) is 3.14 μm and therefore the peak intensity of the underlying buffer peak is much lower than that of the SL0 peak.

The small difference of the angular positions of the buffer and the SL0 peaks confirms the existence of only a very small lattice mismatch between the PbTe QW and the $Pb_{1-x}Eu_xTe$ barriers. With such small mismatches of only 0.19%, the thicknesses of the PbTe quantum wells (for all samples $d_W \leq 120$ Å) is well below the critical layer thickness of this heterosystem, and, therefore, the PbTe layers are fully tensile strained with respect to the $Pb_{1-x}Eu_xTe$ buffer and barriers. This is also evident from the good agreement of the calculated x-ray curve (dashed line in Fig. 1) with the experimental one. From the spacing of the satellite peaks the superlattice period of the MQW stack is obtained. The Eu content in the $Pb_{1-x}Eu_xTe$ layers is calculated from the energy gap determined by infrared transmission measurements (see below) using the relationship between Eu content and the energy gap of $Pb_{1-x}Eu_xTe$ given in Ref. 10. With the knowledge of these two values, the quantum-well thickness was calculated with an accuracy of ±1 Å.

On representative MQW samples, temperature-dependent Hall measurements were performed. Because of the parallel conduction of the $Pb_{1-x}Eu_xTe$ barriers and the buffer layer, the Hall measurements do not directly yield the electrical properties of the PbTe quantum wells. However, the low-temperature mobility of $Pb_{1-x}Eu_xTe$ decreases dramatically with increasing Eu content.[1] In thick single layer reference samples we get 20-K Hall mobilities of about $\mu=700.000$ cm^2/V sec for PbTe, and about a factor of 30 smaller value of $\mu=20.000$ cm^2/V sec for $Pb_{1-x}Eu_xTe$ ($x=3\%$). In both cases the carrier concentration is of an order $n=5\times10^{16}$ cm^{-3}. In MQW samples, we measured 20-K Hall mobilities of the order of $\mu=200.000$ cm^2/V sec. Since the mobilities of the MQW's are of the same order of magnitude as for the PbTe reference layers and are much higher than those of the $Pb_{1-x}Eu_xTe$ reference

layers, it can be concluded that the contribution of the buffer and the barriers to the conductivity in the samples is significantly smaller than the contributions of the PbTe quantum wells. Therefore, the low-temperature mobilities in the quantum wells indeed are of the order of several times 100.000 cm^2/V sec which indicates the high quality of the samples.

The structural parameters of the MQW samples A, B, and C as obtained from the characterization procedures described above are listed in Table I.

B. Midinfrared spectroscopy

Transmission, reflectivity, and photoconductivity measurements in the frequency range from 500 to about 3500 cm^{-1} (corresponding to wavelength of about 3.3–0.5 μm in the high refractive index samples) were performed with the samples mounted in an exchange gas chamber of a temperature variable cryostat equipped with ZnSe windows. A Bruker IFS-113v Fourier transform spectrometer was used with a spectral resolution of 2 cm^{-1}. To ensure photometric accuracy, the sample holder, which could be moved up and down, was equipped with a reference diaphragm identical in size to that used for the sample which was either used to hold a BaF_2 reference sample or a mirror. For the transmission experiments, the rather weak absorption of the BaF_2 substrate was eliminated by normalizing the measured transmission of the MQW samples to that of the BaF_2 substrate. The measurements were performed at $T=5$ and 77 K. For the photoconductivity measurements, a constant current source providing about 1 mA was used, and the voltage drop across the sample was directly fed into a preamplifier and connected to the detector signal input of the Fourier transform spectrometer.

III. TRANSMISSION MEASUREMENTS AND THE FITTING PROCEDURE

The transmission of sample A is shown in Fig. 2(a) for $T=5$ K (dots). The transmission data exhibit Fabry-Pérot interference fringes which result from the refractive index changes at the multilayer stack—vacuum and bulk—substrate interfaces, which are modified by the changes of the optical constants due to various interband absorption processes between confined states in the valence and conduction bands of the MQW structure. The drastic steplike changes in transmission are the consequence of the steplike increases of the absorption constant at the interband transition between confined states. At photon energies above the energy gap of $Pb_{1-x}Eu_xTe$ barriers and buffer (2795 cm^{-1}), the samples become opaque. To deduce the optical constants [$\alpha(\omega)$ and $n(\omega)$] from the measured transmission, a fit to the data was carried out as described below.

A. Absorption coefficient $\alpha(\omega)$

In the strict two-dimensional (2D) case, where the penetration of carrier wave functions into the barriers is negligible, the absorption coefficient in the QW's, taking level broadening into account, is given by[18,19]

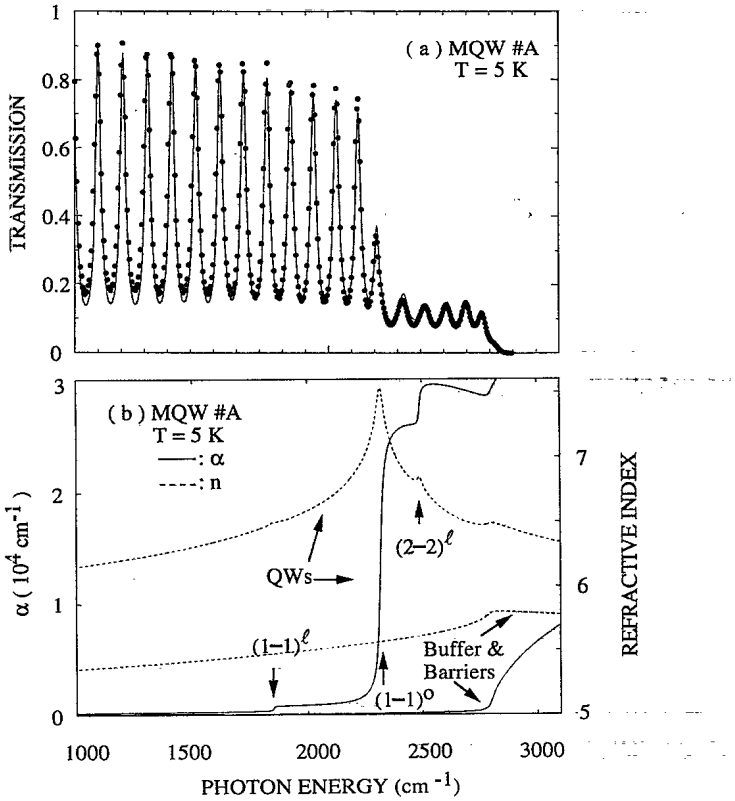

FIG. 2. (a) Transmission vs frequency of MQW sample A. Experimental data, dots; the solid line is the fit based on strict two-dimensional joint density of states. (b) $\alpha(\omega)$ and $n(\omega)$ resulted from the fit.

$$\alpha(\hbar\omega)=\sum_j A_j\frac{1}{\pi}\left[\frac{\pi}{2}+\arctan\left[\frac{\hbar\omega-E_j}{\Gamma_j}\right]\right]\frac{1}{\hbar\omega}\ , \tag{1}$$

where j is the interband transition index, E_j denotes the interband transition energies between the confined states in the VB and in the CB of the PbTe wells, Γ_j is a broadening parameter, $\hbar\omega$ is the photon energy. Since the growth is along [111] direction, two subband systems occur. One is associated with the valley at the L point of the Brillouin zone along the [111] axis (l), which has a circle as surface of constant energy in the (k_x,k_y) plane. The other three valleys, with their main axes oriented obliquely (o) with respect to the [111] growth direction, yield three ellipses as surfaces of constant energy in the two-dimensional case. Consequently, the prefactors A_j, which depend on the two-dimensional joint density of states as well as on the transition matrix elements, are different for the transitions involving subbands of either the longitudinal (l) or oblique (o) valleys:

$$A_j^l=\frac{8\pi e^2}{cn}\frac{2E_p}{\hbar}\frac{1}{4\pi d_w}\times\left[\frac{E_p}{E_j}+\frac{1}{2m_t^c}+\frac{1}{2m_t^v}\right]^{-1} \tag{2}$$

and

$$A_j^o=\frac{8\pi e^2}{cn}\frac{2E_p}{\hbar}\frac{4\bar{\pi}^2+5}{9}\frac{3g_v}{4\pi d_w}\times\left\{\left\{\left[\frac{E_p}{E_j}+\frac{1}{2m_t^c}+\frac{1}{2m_t^v}\right]\times\left[\frac{E_p}{E_j}(1+8\bar{\pi}^2)+\frac{1}{2m_t^c}+\frac{1}{2m_t^v}+8\left[\frac{1}{2m_l^c}+\frac{1}{2m_l^v}\right]\right]\right\}^{1/2}\right\}^{-1} \quad (3)$$

where $g_v(=3)$ is the oblique valley degeneracy index, $E_p=2P_t^2/m_0$ is the square of the transverse interband momentum matrix elements, and $\bar{\pi}=P_t/P_t$ is the ratio of longitudinal to transverse momentum matrix elements.

Equations (2) and (3) are given in cgs units. They differ from the equations used previously by Yuan *et al.*[20] where the far-band contributions to the effective masses $(m_t^c,m_l^c,m_t^v,m_l^v)$ were not taken into account. Similar expressions were obtained in Ref. 21 for IV-VI compound QW's. At this stage, $n(\omega)$ is still an unknown quantity; it will be determined later.

The total dielectric function ϵ^{tot} contains background contributions ϵ^{BG} due to the lattice polarizability and due to various interband transitions other than the fundamental transition at the minimum-energy gap, both from more distant levels at the L points of the BZ (far-band contributions) as well as from the remainder of the BZ. In addition, ϵ^{tot} includes a pronounced dependence on the transitions between the confined states in the valence- and conduction-band extrema. This will be properly calculated in Sec. V and give rise to a contribution $\delta\epsilon^{\text{VB-CB}}$, i.e., $\epsilon^{\text{tot}}=\epsilon^{\text{BG}}+\delta\epsilon^{\text{VB-CB}}$.

B. Refractive index $n(\omega)$

From $\alpha(\omega)$ as calculated from Eq. (1), $\delta\epsilon_2^{\text{VB-Cb}}$ is obtained by using $\delta\epsilon_2^{\text{VB-CB}}=(cn/\omega)\alpha$:

$$\delta\epsilon_2^{\text{VB-CB}}(\hbar\omega)=\sum_j B_j\left[\frac{\pi}{2}+\arctan\left[\frac{\hbar\omega-E_j}{\Gamma_j}\right]\right]\times\frac{1}{(\hbar\omega)^2}\ , \quad (4)$$

where $B_j=c\hbar n A_j$ and c is the velocity of light. It should be noticed that $\delta\epsilon_2^{\text{VB-CB}}$ is independent of n, since it cancels the n in the denominator of A_j in Eqs. (2) and (3).

The expressions

$$\epsilon^{\text{tot}}=\epsilon_1^{\text{tot}}+i\epsilon_2^{\text{tot}}=(\epsilon_1^{\text{BG}}+\delta\epsilon_1^{\text{VB-CB}})+i(\epsilon_2^{\text{BG}}+\delta\epsilon_2^{\text{VB-CB}}) \quad (5)$$

are used in the following. The real part $\delta\epsilon_1^{\text{VB-CB}}$ is calculated from $\delta\epsilon_2^{\text{VB-CB}}$ by the Kramers-Kronig transformation:[22]

$$\delta\epsilon_1^{\text{VB-CB}}=\frac{2}{\pi}P\int_0^\infty d\omega'\omega'\delta\epsilon_2^{\text{VB-CB}}(\omega')/(\omega'^2-\omega^2)\ . \quad (6)$$

Similar to our previous work on PbTe and $Pb_{1-x}Eu_xTe$ epilayers,[10] in the range from 500 to 3500 cm^{-1} we neglect ϵ_2^{BG} and treat ϵ_1^{BG} as a quadratic function of photon energy to account for the contribution of absorptions at critical points other than that at the fundamental absorption. $\epsilon_1^{\text{BG}}(\omega)$ was determined from fits to the experimental transmission spectra of PbTe and $Pb_{1-x}Eu_xTe$ ($x=3\%$) epilayers. We found that in the range from 500 to 3500 cm^{-1}, the expression $\epsilon_1^{\text{BG}}=28.4+4.2\times10^{-7}(\hbar\omega)^2/(cm^{-1})^2$ holds for PbTe and $\epsilon_1^{\text{BG}}=24.3+2.5\times10^{-7}(\hbar\omega)^2/(cm^{-1})^2$ for $Pb_{1-x}Eu_xTe$ with $x=3\%$. For the samples A and C with slightly different Eu content, interpolated values between 28.4 and 24.3, and 4.2×10^{-7} and 2.5×10^{-7}, respectively, were used according to the Eu content. Since ϵ_1^{BG} excludes the contribution from the fundamental absorption at the minimum gap, it is not identical to high-frequency dielectric constant ϵ_∞.

Then the refractive index n and the absorption constant α of the PbTe wells are obtained from[22]

$$n(\omega)=\left\{\epsilon_1^{\text{tot}}\frac{(\omega)}{2}+\tfrac{1}{2}\{[\epsilon_1^{\text{tot}}(\omega)]^2+[\epsilon_2^{\text{tot}}(\omega)]^2\}^{1/2}\right\}^{1/2}, \quad (7)$$

$$\alpha(\omega)=\omega\epsilon_2^{\text{tot}}(\omega)/n(\omega)c\ , \quad (8)$$

The n and α of the $Pb_{1-x}Eu_xTe$ barrier and buffer layers were determined from fitting the transmissions of MBE grown $Pb_{1-x}Eu_xTe$ layers with same Eu content as the MQW samples.[10]

C. Fit to the measured transmission spectra

When $\alpha(\omega)$ [and thus the extinction coefficient $\kappa(\omega)$] and $n(\omega)$ are known for the PbTe wells and the $Pb_{1-x}Eu_xTe$ barriers and buffer, the transmission and reflection from the multilayered samples can be calculated using the transfer matrix method which properly matches the electromagnetic fields at all interfaces.[23,24] In a first step, the measured transmissions of samples A, B, and C were fitted using B_j's, E_j's, and Γ_j's as fitting parameters. In Fig. 2(a) such a fit (solid line) is shown for MQW sample A. The absorption coefficients $\alpha(\omega)$ and refractive index $n(\omega)$ for the best fit are shown in Fig. 2(b) for various layers. The transition energies E_j's marked by the arrows are determined with an accuracy of 0.5 meV for the $(1-1)^o$ transition and 1.5 meV for the $(2-2)^l$ and 2.5 meV for the $(1-1)^l$ transitions. The superscripts o and l refer to oblique and longitudinal valleys and the numbers in the parentheses denote the electric subband indices in the CB and VB, respectively. The fitting parameters are listed in Table II.

The refractive index $n(\omega)$ exhibits cusplike features close to photon energies corresponding to the interband transitions in the QW's. At the $(1-1)^o$ interband transition energy, the refractive index n of the PbTe QW's is 34% higher than the corresponding value of $Pb_{1-x}Eu_xTe$ barriers. Similar fits were performed for samples B and C. In Fig. 3, the absorption coefficients

TABLE II. Fitting parameters.

Sample	j	E_j (cm^{-1}/meV)	B_j (10^4 meV^2)	Γ_j (cm^{-1}/meV)
	1	1850/229	0.5	5/0.62
A	2	2317/287	34	10/1.2
	3	2490/309	5.2	5/0.62
	1	1730/214	0.9	10/1.2
B	2	2170/269	22	10/1.2
	3	2900/359	13	10/1.2
	1	1680/208	0.2	10/1.2
	2	2015/250	13	8/1.0
	3	2170/269	2.8	10/1.2
	4	2370/294	0.3	10/1.2

and refractive indices of all samples are plotted together. In accordance with the prediction of Eqs. (2) and (3) that the A_j's (thus B_j's) are inversely proportional to the well width d_w, $\alpha(\omega)$ increases with decreasing well width. Accordingly, the cusplike increases in $n(\omega)$ increase also with decreasing d_w. In Ref. 20 we have shown that without the cusplike enhancement of $n(\omega)$ in the frequency range close to the interband transitions, the calculated spectra differ from the measured spectra, i.e., the Fabry-Pérot fringes are shifted.

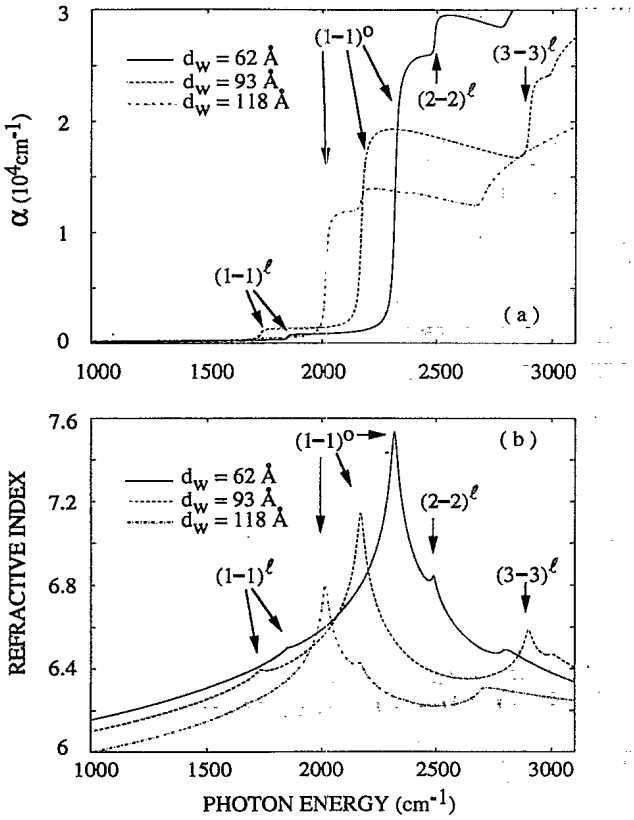

FIG. 3. (a) Absorption coefficient $\alpha(\omega)$ of PbTe QW's determined by the fit procedure for MQW samples A,B, and C. Subband absorption is assumed to take place only in the PbTe wells for photon energies below the energy gap of the $Pb_{1-x}Eu_xTe$ barriers and buffer. (b) Corresponding refractive index $n(\omega)$ obtained from $\alpha(\omega)$ as described in text.

IV. ELECTRONIC PROPERTIES AND BAND OFFSETS OF PbTe/$Pb_{1-x}Eu_xTe$ HETEROSTRUCTURES

A. Band-structure calculation

It is well known that up to Eu contents of about 5% the band structure of $Pb_{1-x}Eu_xTe$ is similar to that of PbTe. Both have a minimum direct gap at the L points of the Brillouin zone. Consequently, the superlattice (SL) band structure in the vicinity of the band extrema is most readily calculated via the envelope function approximation.[25] This requires the knowledge of the band gaps, their alignments, the interband momentum matrix elements as well as the far band parameters.

Because of the many-valley band structure, the EFA calculation is somewhat different from the usual calculation of the SL band structure of III-V or II-VI compounds,[18,22] which have their band extrema at the Γ point of the BZ. In addition, the different orientation of the valley axes with respect to the growth direction requires a transformation between the coordinate axes. So far no indication has been found for a coupling of different valleys caused by the interfaces.[7] In the following the essential features of this EFA calculation are presented, because the results are needed for the evaluation of the absorption coefficient and the refractive index later on. It should be noted that a superlattice composed of IV-VI materials still has a center of inversion and thus the eigenvalues are all doubly degenerate.

For energy states close to the band edges, the EFA theory, which takes into account the twofold degeneracy of CB and VB explicitly and the far-band contributions in second-order perturbation theory, suffices for a description of energy eigenstates and optical properties. Thus the Hamiltonian has, due to symmetry requirements (the conduction band has symmetry L_6^- and the valence band L_6^+), the form

$$H=\begin{bmatrix} h_{cc} & h_{cv} \\ h_{vc} & h_{vv} \end{bmatrix}, \tag{9}$$

where

$$h_{cc}=\left[E_c+k_t\frac{\hbar^2}{2m_0m_t^c}k_t+k_3\frac{\hbar^2}{2m_0m_l^c}k_3 + D_d^c\mathrm{Tr}\epsilon+D_u^c\epsilon_{33}\right]I_{22}, \tag{10}$$

$$h_{cv}=h_{vc}=\begin{bmatrix} \{P_lk_3\} & \{P_t(k_1-ik_2)\} \\ \{P_t(k_1+ik_2)\} & -\{P_tk_3\} \end{bmatrix} \tag{11}$$

and $h_{vv}=h_{cc}$ with the index c replaced by v. $\{AB\}=\frac{1}{2}(AB+BA)$.

In the above formula, I_{22} denotes a 2×2 unity matrix, E_c and E_v denote the CB and VB edges, ϵ is the strain tensor, and D_d and D_u are the deformation potentials.[7]

The only effect of strain in the material is a shift of the band edges. $k=-i\nabla$, the indices 1,2,3 refer to a Cartesian coordinate system for each valley orientation with 3 denoting the main valley axis. It is related to the SL coordinate system (z parallel to the growth direction) by the transformation matrix T:

$$\begin{bmatrix} k_1 \\ k_2 \\ k_3 \end{bmatrix} = T \begin{bmatrix} k_x \\ k_y \\ k_z \end{bmatrix} . \tag{12}$$

The eigenstates are obtained by the solution of the four coupled differential equations

$$Hf = Ef , \tag{13}$$

where $f=(f_1,f_2,f_3,f_4)$.

In the past the question of matching conditions at the interface between two layers of piecewise solutions for the individual bulk layers arose much interest. This difficulty can be avoided, however, by assuming a more gradual continuous transition between two layers,[7] as it probably reflects the actual physical situation anyway, where monolayer fluctuations are known to occur from our scanning tunneling microscopy investigations. Then Eq. (13) is a set of coupled differential equations with analytic coefficients and has analytic solutions.[7] If the EFA treatment is expected to give meaningful results, the actual transition layer width which is much smaller than the layer width must have a negligible influence on the results.

A superlattice composed of IV-VI compounds, for which the EFA Hamiltonian as given in Eq. (9) holds, is described[7] by the Hermitian eigenvalue problem Eq. (13). However, the material parameters, especially the band-edge energies E_c and E_v are not constant, but position dependent. The superlattice is periodic in D, the sum of the individual layer thickness ($D=d_w+d_b$). This implies a Bloch condition

$$f_b(z+D)=\exp(ikD)f_b(z) , \tag{14}$$

thus introducing a Bloch number K (or superlattice wave vector). z denotes the direction perpendicular to the individual layers. In the directions x,y parallel to the layers the material parameters are constant and thus the solutions to Eq. (13) are given as

$$f_b(x,y,z)=\exp(ik_x x)\exp(ik_y y)Z_b(z) , \tag{15}$$

where the functions Z_b obey the conditions of Eq. (14). The solutions are thus characterized by the three quantum numbers (k_x,k_y,K). The coupled differential equations for the functions Z_b in the variable z have to be solved next. This is achieved by an expansion in B splines[26] and the differential equation is transformed in a generalized Hermitic eigenvalue problem. By a suitable choice of node points, the dimension of the Hermitic matrix can be kept quite low (typical 20 node points per layer). This method also yields good eigenfunctions and therefore allows to calculate optical properties.

In the following, we present an example for the energy dispersion of a PbTe/$Pb_{1-x}Eu_xTe$ MQW sample using the parameters given in Table III. For the dependence of the energy gap on Eu content, the empirical relation of Partin[1] for $Pb_{1-x}Eu_xSe_yTe_{1-y}$ in the modification of Yuan *et al.*[10] for $Pb_{1-x}Eu_xTe$ was used:

$$E_g(x,T)\ (\text{meV}) = 190+0.51\ T^2(\text{K})^2(1-9.8x)/[T(\text{K})+56] + 5880x . \tag{16}$$

Recently, Karczewski *et al.*[27] have reported that the mass anisotropy of electrons and holes changes in $Pb_{1-x}Eu_xTe$ in comparison to PbTe. The EFA band-structure calculations were performed for two sets of parameters, either using for $Pb_{1-x}Eu_xTe$ the interband momentum matrix elements P_t and P_l as given by Karczewski *et al.*[27] or leaving these parameters identical to PbTe.[28,29] For the calculation of confined states in the PbTe wells of MQW's, the change of the interband momentum matrix elements has only a minor influence on these energies as long as the carrier wave functions are sufficiently confined in PbTe and do not extend too much into the $Pb_{1-x}Eu_xTe$ barriers. For the far-band masses m_t^c,m_l^c,m_t^v,m_l^v identical values were used for PbTe and $Pb_{1-x}Eu_xTe$.

In Fig. 4, the calculated energy dispersion $E(k_x,k_y,K)$ is shown for MQW sample B with a PbTe well width of $d_W=93$ Å, a $Pb_{1-x}Eu_xTe$ barrier width of $d_B=554$ Å, and $x=3\%$. The dispersion is shown both for the longitudinal valley [111] and for the three oblique valleys $[11\bar{1}]$ for a normalized offset of $\Delta E_c/\Delta E_g=0.55$. The superlattice vector K is directed along growth direction [111]. The in-plane dispersion is shown as a function of k_x,k_y for the valley $[11\bar{1}]$ with $k_x \| [\bar{1}10]$ (solid line) and $k_y \| [1\bar{1}2]$ (dashed line) for $K=0$ and $k=-\pi/D$. In contrast to the bulk band structure, for the k_y direction in the MQW band structure a noncrossing behavior occurs.

B. Band offsets

In order to determine the band offsets, the experimentally obtained transition energies (see Table II) are com-

TABLE III. Band parameters of bulk PbTe and $Pb_{1-x}Eu_xTe$.

	E_g (meV)	$2P_\perp^2/m_0$ (eV)	$P_\perp/P_\parallel$	m_t^c/m_0	m_l^c/m_0	m_t^v/m_0	m_l^v/m_0
PbTe[a]	189.7	6.02	3.42	0.060	0.505	0.102	0.920
$Pb_{1-x}Eu_xTe$[b]	Eq. (16)	8.23	3.86	0.060	0.505	0.102	0.920

[a]References 28 and 29.
[b]Reference 27.

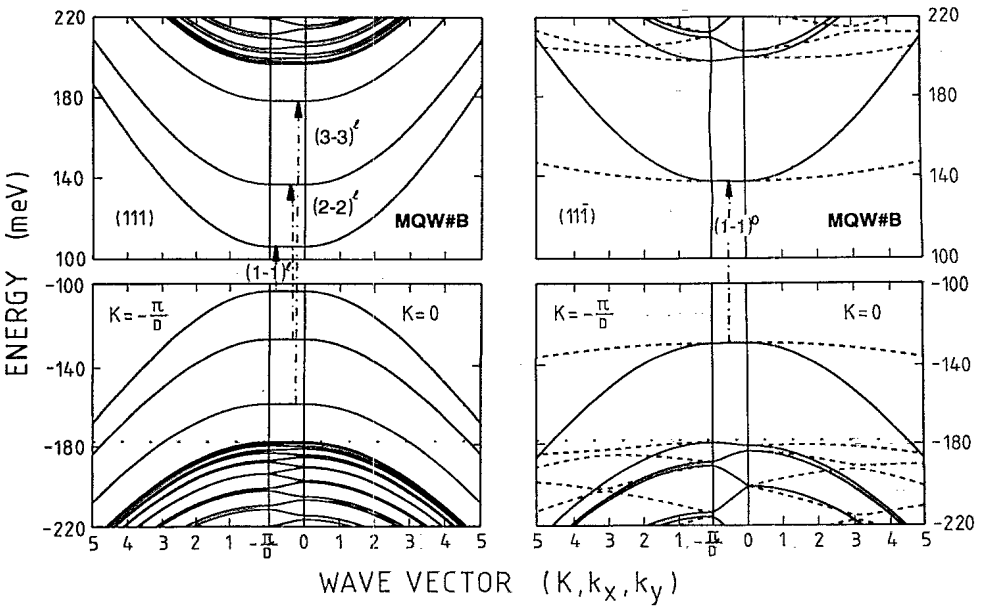

FIG. 4. Energy-momentum relationship for MQW B for the longitudinal (111) valley (left-hand side) and oblique (11$\bar{1}$) valley calculated from EFA. The dispersion along the superlattice growth direction (between $K=0$ and $-\pi/D$) is shown, as well as the dispersion as a function of the $k_x \| [1\bar{1}0]$ and $k_y \| [11\bar{2}]$ directions (full line and dashed lines, respectively). The transitions between subbands are indicated by arrows.

pared with those calculated on the basis of the EFA model assuming a wide range of band offsets from $\Delta E_c/\Delta E_g = -0.5-1.5$, i.e., including a staggered band line up. ΔE_c is the conduction-band offset and is positive if the conduction band of $Pb_{1-x}Eu_xTe$ lies above that of PbTe. ΔE_g is given by $E_g(Pb_{1-x}Eu_xTe) - E_g(PbTe)$, i.e., it is positive.

In Fig. 5, the calculated transition energies are plotted vs the normalized offset $\Delta E_c/\Delta E_g$ MQW sample A data at 5 and 77 K. The full lines in Fig. 5 correspond to the experimental transition energies. For the two other samples, the same is shown in Figs. 6 and 7 where on the left-hand side of the figures the transitions within the longitudinal valley subband systems are shown and on the right-hand side the oblique one. The different symbols (squares, circles, triangles, and crosses) indicate different oscillator strengths decreasing stepwise by a factor of 2 from squares, circles, triangles, and crosses. For the lowest transition $(1-1)^l$ the variation of its transition energy with the conduction-band offset is rather small. However, for the transitions involving carriers in the oblique valleys or for the transitions between higher subbands of the longitudinal valley, the transition energies vary strongly with band offset. From the comparison with the experimental values for all samples, we conclude that the normalized CB offset $\Delta E_c/\Delta E_g$ is 0.55 ± 0.2. In addition, from Fig. 5 it is concluded that the band offset does not change with temperature at least up to 77 K.

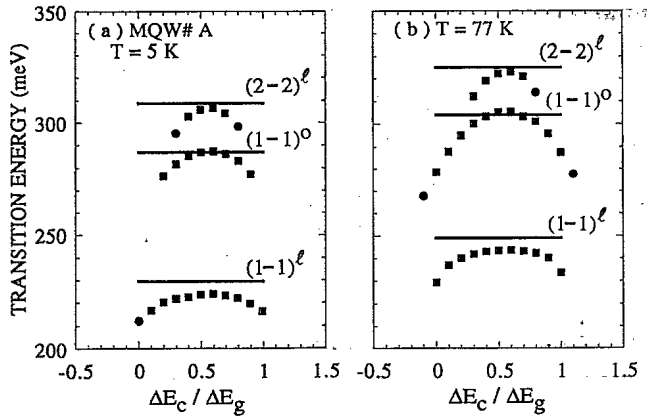

FIG. 5. Calculated transition energies for the $(i-i)^{l,o}$ transitions as a function of the normalized band offset $\Delta E_c/\Delta Eg$ for MQW A for (a) $T=5$ K and (b) $T=77$ K. Symbols (squares, circles, triangles, and crosses indicate different oscillator strength, decreasing stepwise by a factor of 2), calculation; full lines, experimental data.

V. OPTICAL PROPERTIES: A COMPARISON OF EXPERIMENTAL AND EFA CALCULATED TRANSMISSION AND REFLECTIVITY DATA

To our knowledge, most of the transmission and reflectivity experiments performed with MQW systems and superlattices so far have mainly been interpreted by assuming that the optical constants $n(\omega)$ and $\alpha(\omega)$ of the wells and the barriers change abruptly at the interfaces

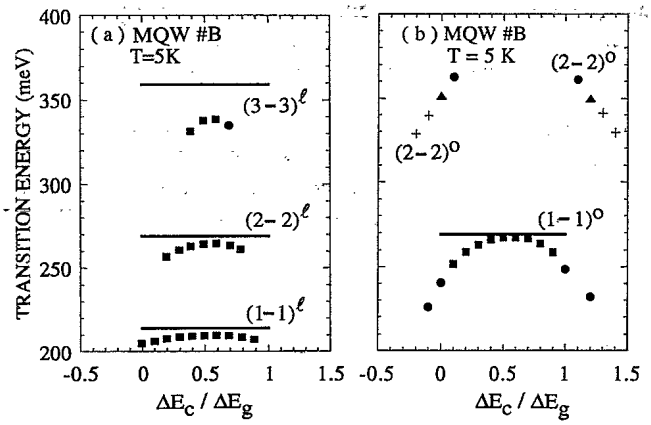

FIG. 6. Same as Fig. 5, but for MQW B.

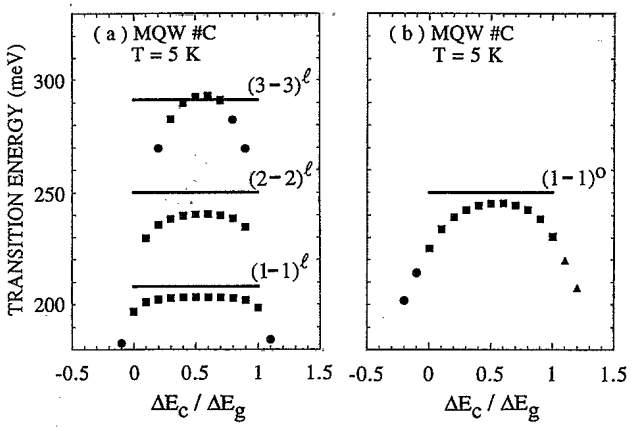

FIG. 7. Same as Fig. 5, but for MQW *C*.

and vary periodically along the growth direction with a period determined by the well and barrier layer widths.[23,24] In the QW's, MQW's, and SL's, the electronic intraband as well as interband transitions contribute to $n(\omega)$ and $\alpha(\omega)$.[22] However, in narrow-gap materials the carrier wave functions extend appreciably into the barriers. In addition, also within the well, the carrier density depends considerably on the z coordinate. Consequently, the contributions from the electronic transitions to the optical constants in QW's, MQW's, and SL's are *not piecewise constant* in the wells and barriers. This is especially true for SL's.

As the midinfrared electromagnetic wave extends over many PbTe wells and $Pb_{1-x}Eu_xTe$ barrier layers, the $PbTe/Pb_{1-x}Eu_xTe$ MQW's can be treated as a virtually homogeneous material concerning the electronic contribution $\delta\epsilon^{\text{VB-CB}}$ to the optical constants, i.e., absorption occurs throughout the entire period of the multiple-quantum-well structure. We denominate this approach the EFA-SL model.

On the other hand, even in a recent book on QW lasers,[30] a lengthy discussion on the conceptional aid of using the physical well width d_W for a description of the absorption was presented. In the spirit of that discussion, we renormalize the $\alpha^{\text{SL}}(\omega)$ calculated from the EFA-SL model to the well width using $\alpha^{\text{QW}}(\omega)=\alpha^{\text{SL}}(\omega)D/d_W$ and present the results too. The latter method is denominated the QW model.

In the following, we present the calculated transmission and reflection using the EFA-SL model and QW-model and compare the results with the experimental spectra. In this context, we need the QW model in order to compare the results on $\alpha(\omega)$ and $n(\omega)$ directly with $\alpha(\omega)$ and $n(\omega)$ from the fits shown in Sec. III. The CB offset was taken to be $0.55\Delta E_g$ as determined in Sec. IV.

A. Transmission and reflectivity using the EFA-SL model

In this model, the interband absorption between the electronic subbands of the VB and CB is assumed to occur throughout the whole $PbTe/Pb_{1-x}Eu_xTe$ MQW's, not only in the PbTe QW's. Only the background dielectric functions ϵ_1^{BG}'s are assumed to be different for the PbTe wells and the $Pb_{1-x}Eu_xTe$ barriers in the evaluation of the Fabry-Pérot problem via the transfer matrix method. In the calculation, automatically the number of periods in the MQW's enters. We used the EFA not only to calculate the E_j's but also to calculate $\alpha(\omega)$ directly from the EFA wave function:

$$\alpha(\omega)=\frac{4\pi^2e^2}{c\omega n}\frac{1}{(2\pi)^3}\int d\mathbf{k}\,\delta(E_f-E_i-\hbar\omega)|\langle f|\dot{r}_E|i\rangle|^2\times(f_i-f_f)\,, \tag{17}$$

hence

$$\delta\epsilon_2^{\text{VB-CB}}=(cn/\omega)\alpha=\frac{4\pi^2e^2}{\omega^2}\frac{1}{(2\pi)^3}\int d\mathbf{k}\,\delta(E_f-E_i-\hbar\omega)|\langle f|\dot{r}_E|i\rangle|^2\times(f_i-f_f)\,, \tag{18}$$

where E_i, E_f denote the energies of the initial state (i) and final state (f), and f_i, f_f the Fermi-Dirac distribution functions for the occupancy of the initial and final states. We emphasize that the refractive index n in Eq. (17) cancels out in the expression for $\delta\epsilon_2^{\text{VB-CB}}$ in Eq. (18).

In the EFA the velocity operator is given by

$$\dot{\mathbf{r}}=\frac{1}{i\hbar}[\mathbf{r},H]=\frac{1}{\hbar}\frac{\partial H}{\partial\mathbf{k}}\,. \tag{19}$$

Equation (18) was evaluated numerically for the three MQW samples by calculating their energy dispersion and wave functions for a sufficient number of points in the (k_x,k_y,K) space. The $\mathbf{k}$ integration was performed using the Lehmann-Taut tetraeder scheme.[31]

The $\alpha(\omega)$ and $n(\omega)$ used for the calculations were finally obtained in the same way as described by Eqs. (5)–(8) in Sec. III B. In Fig. 8(a), the calculated transmission for MQW sample A is compared with the experimental spectrum. The calculation is based on $\alpha(\omega)$ and $n(\omega)$ according to Eqs. (18), (8), and (7), i.e., based on the EFA analysis together with the numerical $\mathbf{k}$ integration over all interband transitions between the subbands. $\delta\epsilon_2^{\text{VB-CB}}$ is the same for the PbTe well and $Pb_{1-x}Eu_xTe$ barrier layers. The overall higher refractive index for the PbTe layers in comparison to that of the $Pb_{1-x}Eu_xTe$ barriers is due to the higher background dielectric function ϵ_1^{BG}. Otherwise $n(\omega)$ has a similar functional dependence on $\hbar\omega$ both for the wells and the barriers, i.e., showing the cusplike increase at photon energies corresponding to the various interband transitions. The difference in the absolute values of $n(\omega)$ between the buffer and barrier layers results from the influence of the interband transitions within the MQW structure, which manifest themselves through the Kramers-Kronig transformation also in the refractive index. Above the energy gap of the $Pb_{1-x}Eu_xTe$ layers α increases strongly and the Kramers Kronig related quantity $n(\omega)$ shows a maximum.

In Fig. 9, we show similar experimental data and calculations of the transmission vs photon energy for the MQW samples B and C, which have wider PbTe well widths. For all three MQW samples the calculated

transmission data, i.e., both the magnitude and the phase of the Fabry-Pérot fringes, are in good agreement with the experimental data. In the EFA calculation just bulk band parameters and the experimentally determined structural parameters (layer thicknesses and Eu content) were used. We emphasize that in the calculation for the transmission of the MQW's, *no adjustable parameter* enters once the band offset has been fixed.

A comparison of the calculated $\alpha(\omega)$ and $n(\omega)$ for the three MQW's is shown in Fig. 10. Because of the threefold valley degeneracy, the differences in joint density of states masses and in the transition matrix elements, in all three samples the transition $i=1$ (VB) to $i=1$ (CB) within the oblique valley subband ladders $(1-1)^o$, leads to an $\alpha(\omega)$ which is by a factor of about 5 larger than those for the longitudinal valley transitions $(1-1)^l$, $(2-2)^l$. As a consequence, the strong increase in $\alpha(\omega)$ at $(1-1)^o$ transitions leads also to the highest cusp in $n(\omega)$, whereas those associated with the longitudinal valley $[(1-1)^l(2-2)^l,(3-3)^l]$ are substantially weaker and lead correspondingly to smaller cusps in $n(\omega)$. The general "background" trend in the $n(\omega)$'s on which the cusps are superimposed is determined by the Eu content of the barrier layers: the higher the Eu content, the smaller the refractive index apart from the regions where the cusplike

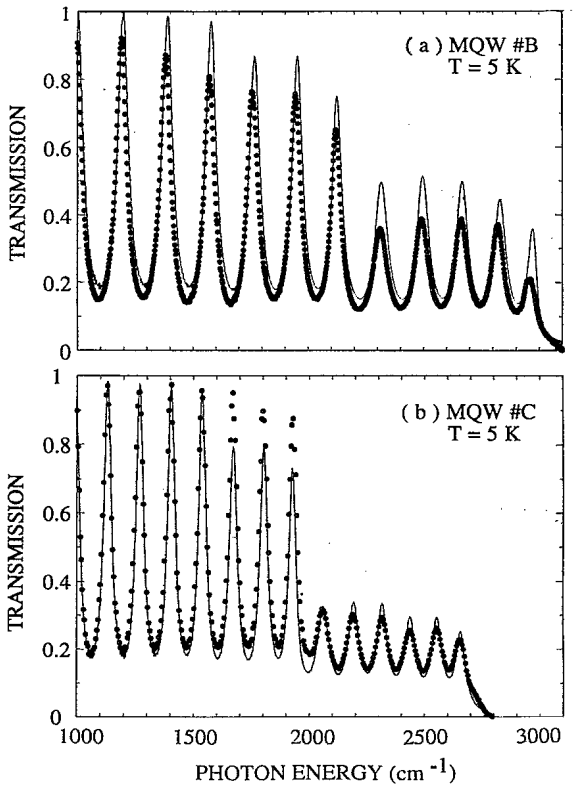

FIG. 9. Transmission vs frequency for MQW (a) *B* and (b) *C*. Dots, experimental data; full lines, calculations using the EFA-SL model.

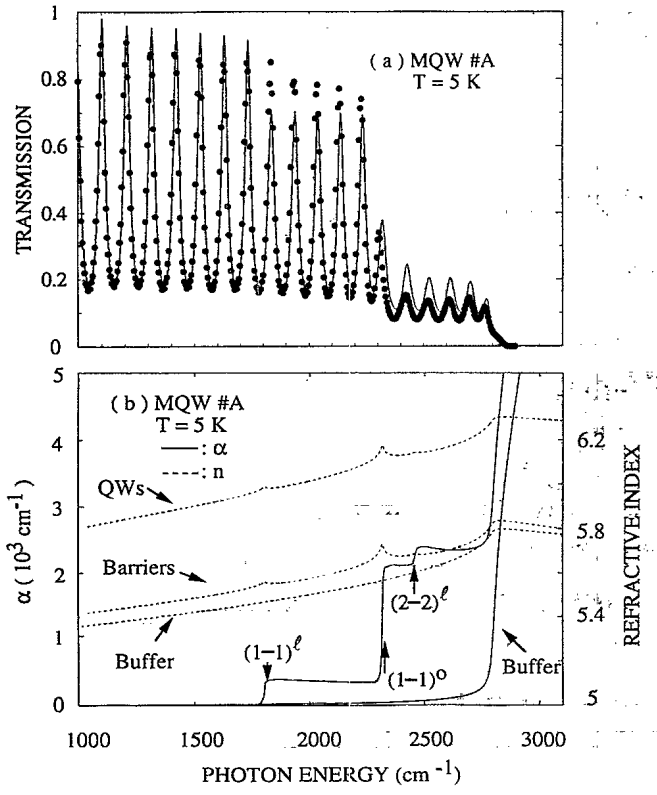

FIG. 8. (a) Transmission vs frequency for MQW sample *A*. Dots, experimental data at $T=5$ K; full line, calculation using the EFA-SL model. (b) Frequency dependence of the calculated absorption constant $\alpha(\omega)$ (full lines) and of the refractive index $n(\omega)$ for various layers. The arrows indicate interband transitions between subbands associated with longitudinal (l) and oblique (o) valleys.

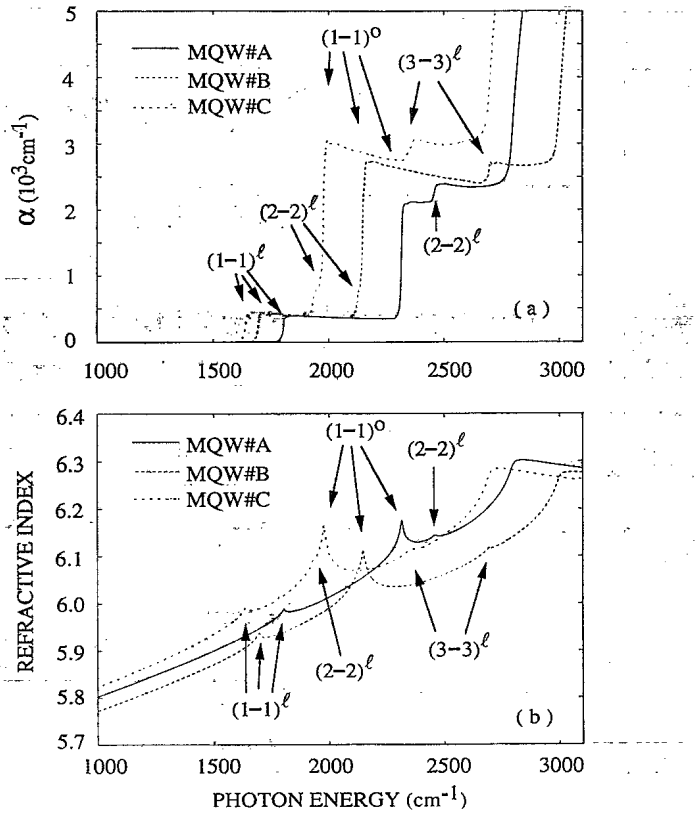

FIG. 10. (a) Comparison of $\alpha(\omega)$ of the $PbTe/Pb_{1-x}Eu_xTe$ MQW's calculated using the EFA-SL model; (b) refractive index $n(\omega)$ for the three MQW samples. Interband transitions involving longitudinal and oblique valleys are indicated by arrows.

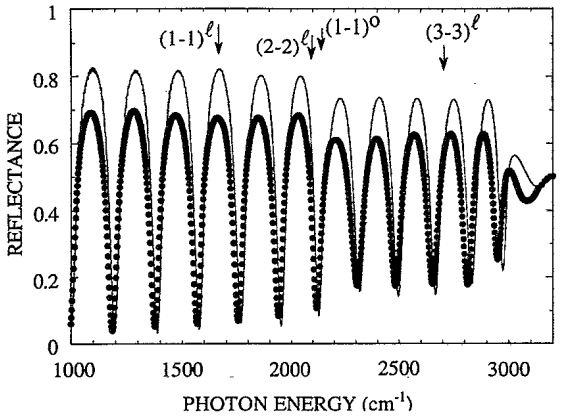

FIG. 11. Reflectivity spectra of MQW B. In the calculation, $\alpha(\omega)$ and $n(\omega)$ are taken from Fig. 10. Measurements, dots; calculation, solid line.

enhancements occur.

Despite the fact that in the transmission data, due to the use of a multilayer stack deposited on a cleaved substrate, Fabry-Pérot fringes occur and thus in the transmission data information on the reflectivity is already contained, we also measured as a check of the analysis the reflectivity for MQW sample B at $T=5$ K (Fig. 11, dots). Using the $n(\omega)$ and $\alpha(\omega)$ given in Fig. 10, the corresponding reflectivity spectrum was calculated and is shown in Fig. 11 (solid line). The transition energies of the $(i-i)^{l,o}$ transitions are indicated by arrows. Apart from photon energies close to the $Pb_{1-x}Eu_xTe$ gap, the phases of the interference fringes in the reflectivity spectrum are well accounted for. Close to the $(1-1)^o$ transition energy, the largest change in $R(\omega)$ occurs. The overall agreement between the calculated data and the experiments can be considered to be satisfactory, having in mind that no adjustable parameter has been used.

B. Transmission calculated using the QW model

In the evaluation of the transition data in Sec. III, it was assumed that the electrons are located in the PbTe well layers, and thus that absorption takes place in the wells only. The QW model is based on the same assumption. Consequently, we apply the transfer matrix method in the sense that we use $\alpha^{SL}(\omega)$ according to the Eq. (17) but normalize it to the well width, i.e., $\alpha^{SL}(\omega)D/d_W$. Further we assume that the barrier layers do not absorb below their energy gaps, i.e., for the barrier layers the same $n(\omega)$ and $\alpha(\omega)$ as for the buffer layer are used. This approach is useful for a comparison of the optical constants obtained from the fit to the measured spectra (Sec. III) with the EFA calculations (Sec. V A). The such calculated transmission is shown in Fig. 12 together with the corresponding $\alpha(\omega)$ and $n(\omega)$ for MQW sample A. Since in this case the absorption is deliberately restricted to the PbTe quantum wells, the corresponding absorption constant is much larger than that shown in Fig. 8(b), and consequently the steplike changes of $\alpha(\omega)$ are larger.

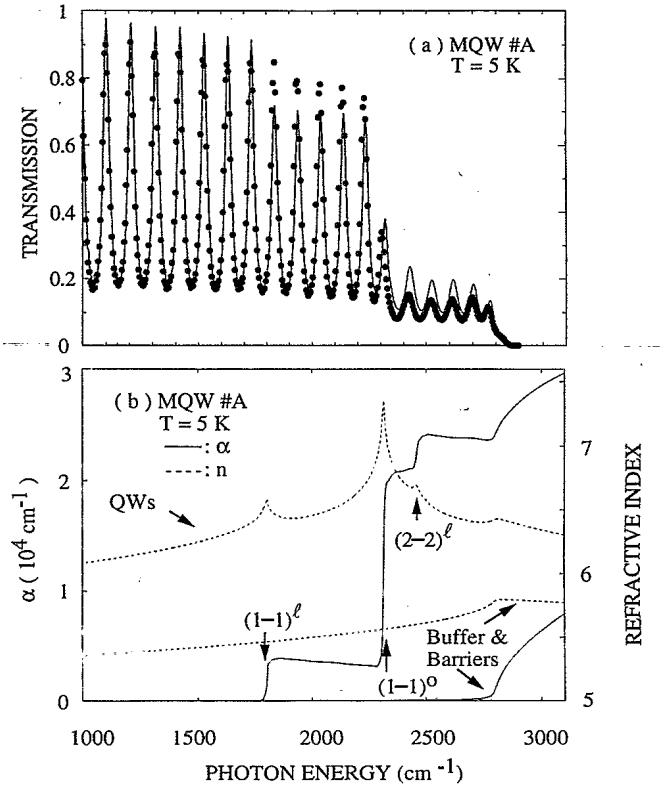

FIG. 12. (a) Transmission vs frequency for MQW sample A, at $T=5$ K. Dots, experimental data; full line, calculation using the QW model. (b) Calculated absorption constant $\alpha(\omega)$ (full lines) and refractive index $n(\omega)$ (dashed lines) for QW, barrier, and buffer layers using the QW model.

Therefore the corresponding refractive index $n(\omega)$ exhibits much larger cusps at the transition energies $(i-i)^{l,o}$ than those shown in Fig. 8(b). At the $(1-1)^o$ transition energy, $\Delta n/n$ is as large as 30% with respect to the refractive index of the barrier layer, in comparison to 9% in Fig. 8(b).

In Fig. 13, the results on $\alpha(\omega)$ and $n(\omega)$ are summarized for the three samples in order to show the systematic changes of $\alpha(\omega)$ and $n(\omega)$ with the PbTe well width d_W in this model calculation. The smaller d_W, the larger the steplike increase of $\alpha(\omega)$ near the interband transitions between confined states $(i-i)^{l,o}$ and the larger the cusps in $n(\omega)$.

For a comparison of the calculated $\alpha(\omega)$ and $n(\omega)$ with those obtained from the fitting procedure described in Sec. III, in Fig. 14 both pairs of optical constants for MQW A are plotted. The calculated steplike increase of $\alpha(\omega)$ is somewhat larger for frequencies at the onset of the $(1-1)^l$ transition but smaller for the $(1-1)^o$ transition as compared with the values obtained from the fitting procedure. However, the overall agreement is quite reasonable. For the refractive index, the enhancement of $n(\omega)$ close to the $(1-1)^o$ transition which follows from the fit is somewhat larger than the one calculated from the EFA model. Apart from these small deviations and slight discrepancies of the transition energies the overall agreement between the frequency dependence

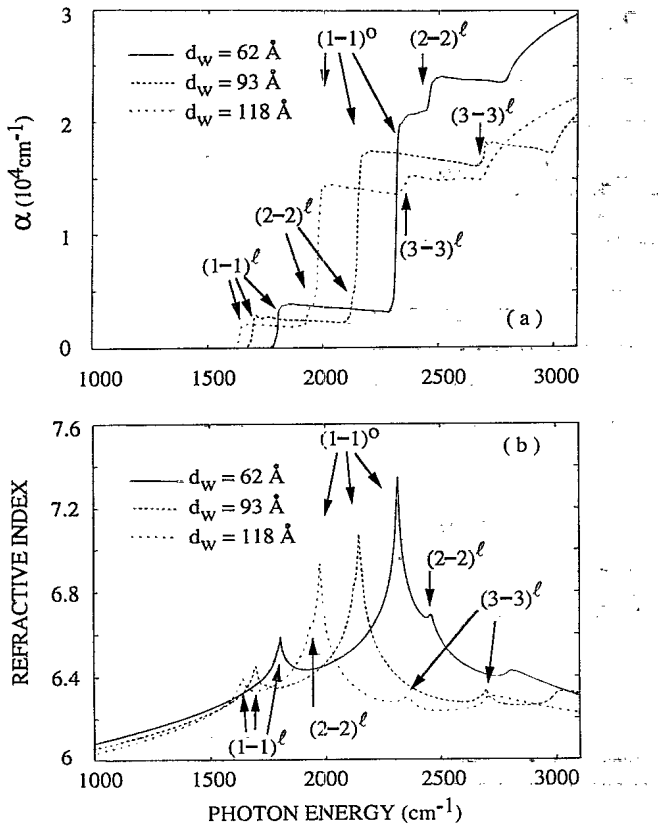

FIG. 13. (a) Comparison of QW absorption constants $\alpha(\omega)$ evaluated using the QW model for the three samples investigated (MQW samples *A*, *B*, and *C*); (b) refractive index $n(\omega)$.

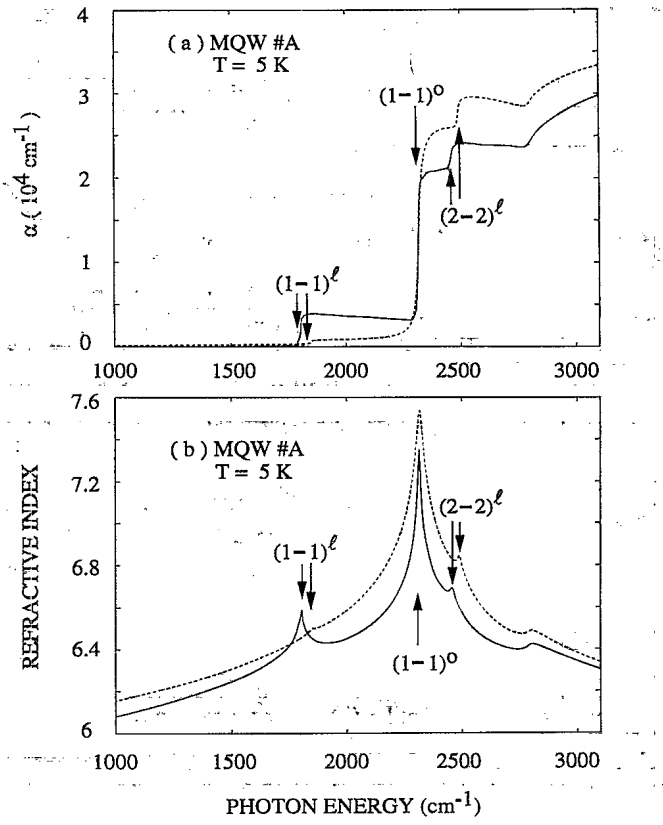

FIG. 14. (a) Comparison of $\alpha(\omega)$ determined from the QW model calculation (full line) with $\alpha(\omega)$ from the fit to the experimental transmission data (dashed line) for MQW *A*. (b) Refractive indices $n(\omega)$ determined by Kramers-Kronig transformation from corresponding $\alpha(\omega)$ shown in the upper panel.

of $\alpha(\omega)$ and $n(\omega)$ derived from the fit and those derived from the EFA-based QW model calculation is remarkably good.

C. Photoconductivity measurements

As a further check, photoconductivity (PC) measurements as a function of photon energy were made on all samples, and an example is shown in Fig. 15 for MQW sample *A*. The photoconductivity normalized to the transmitted intensity is directly related to the changes in $\alpha(\omega)$. Indeed, the PC signal shown in Fig. 15 exhibits steplike increasing at the onsets of the $(1-1)^l$ and $(1-1)^o$ transitions. Increasing the lattice temperature from 5 to 77 K, the PC onsets shift in agreement with the temperature dependence of the PbTe and $Pb_{1-x}Eu_xTe$ energy gaps. The wiggles on the plateaus of the photoconductivity signal result from the Fabry-Pérot fringes in the transmission signal. The slight shift of the onset of the $(1-1)^l$ transition in the PC spectrum with respect to the calculated $\alpha(\omega)$ results from the finite number of electrons occupying the $j=1^l$ confined state in the conduction band. In contrast, for the $(1-1)^o$ transition involving the unoccupied $j=1$ levels in oblique valleys, the PC onset agrees exactly with the calculation. In agreement with the calculated $\alpha(\omega)$, the step in the PC signal is much larger for the $(1-1)^o$ transition than for the $(1-1)^l$ transition, reflecting the threefold valley degeneracy and the higher joint density of the states for the transitions involving the oblique valleys.

VI. DISCUSSION

In the frequency range investigated, the wavelength of the light is about an order of magnitude larger than the

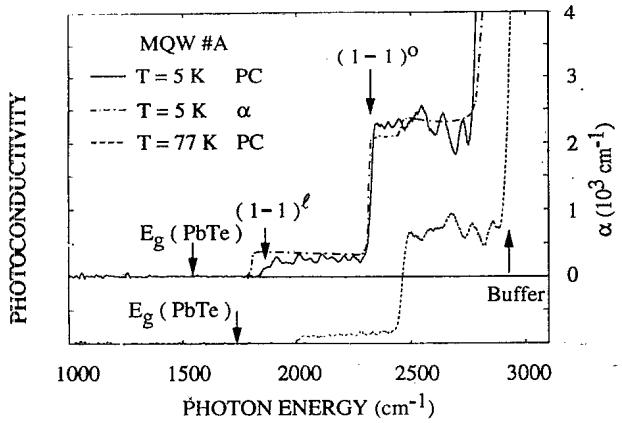

FIG. 15. Photoconductivity vs frequency of MQW sample *A* at $T=5$ K (solid line) and 77 K (dashed line) and calculated $\alpha(\omega)$ (EFA-SL model) with transitions indicated by arrows.

$PbTe/Pb_{1-x}Eu_xTe$ MQW periods. Indeed, the fringes in the transmission spectrum arise mainly from multiple reflections and interference effects in the whole multilayer stack including the buffer of several micrometers thickness and are only modified by the interference effects *within* the MQW parts of the samples.

It was shown in Sec. V that the calculation of the transmission and reflectivity spectra of these MQW systems based on the EFA wave functions and a numerical **k** integration, which yields the electronic contributions to $\alpha(\omega)$ and through Kramers-Kronig transformation also $n(\omega)$, reproduces the measured spectra on all samples quite well, even though no adjustable parameters were used once the band offset was fixed.

The conventional QW method used for evaluating the absorption constant, assuming interband absorption between electronic subbands taking place only within the wells, yields numerical values for $\alpha(\omega)$ and $n(\omega)$ which are quite different in the magnitude from those resulting from the EFA-SL model where the MQW is treated as an optically quasihomogeneous material. This fact follows from the comparison of the optical constants plotted in Figs. 10 and 13. In the conventional picture, the steplike changes in $\alpha(\omega)$ of PbTe QW's are inversely proportional to the well thicknesses and consequently also the cusplike changes in $n(\omega)$ of PbTe QW's which correspond to the steps in $\alpha(\omega)$ scale inversely with the well thickness. The thinner the well the larger the steps in $\alpha(\omega)$ and thus the larger cusps in $n(\omega)$.

In the calculation based on the EFA model and the numerical **k** integration, the corresponding $\alpha(\omega)$ and $n(\omega)$ of the $PbTe/Pb_{1-x}Eu_xTe$ MQW's are not related to the well width but to the MQW period D, and both the steps in $\alpha(\omega)$ of the $PbTe/Pb_{1-x}Eu_xTe$ MQW's and the cusps in $n(\omega)$ of PbTe layers are comparable in their magnitude for all three samples. It should be noticed that in spite of this discrepancy in $\alpha(\omega)$ and $n(\omega)$, both models yield nearly the same calculated transmission spectra. The crucial point is the following: in the QW model with a strictly two-dimensional joint density of states, the electronic contributions $\delta\epsilon^{\text{VB-CB}}$ change abruptly at the interfaces, whereas in the EFA-SL model these contributions are constant throughout the entire MQW stack.

It is obvious that for a staggered band alignment, and even more so for type-II alignment, the calculation of $\alpha(\omega)$ and $n(\omega)$ according to the QW model is not appropriate at all, since the wave-function amplitudes of conduction and valence bands involved in the interband transitions are spatially separated along growth direction. In this case only the EFA-SL model can be used.

The conceptional problem with the description of absorption in a QW arises from the fact that in two dimensions the definition of an absorption coefficient in units of an inverse length is inappropriate. For a strict 2D sheet, there can be a finite absorption, despite the fact that the thickness along the propagating direction of the electromagnetic radiation is zero. In order to obtain an absorption coefficient (in units of an inverse length), the quantity describing the QW absorption has to be divided by a characteristic length for which conventionally the QW thickness d_W is used. In contrast, the EFA-SL-model, which yields $\alpha(\omega)$ due to the electric interband transitions based on the numerical **k** integration over the initial and final states and the appropriate envelope wave functions, gives a *realistic* description of the absorption problems in MQW systems.

VII. CONCLUSION

The frequency dependence of the absorption constants and of the refractive index was investigated experimentally and theoretically in the range of interband transitions between confined states in the valence and conduction band of $PbTe/Pb_{1-x}Eu_xTe$ MQW's. Since this material combination is actually in use for the fabrication of efficient mid infrared diode lasers, information on their optical properties is necessary for a proper design of such lasers. The CB offset of the $PbTe/Pb_{1-x}Eu_xTe$ ($x<5\%$) heterostructures was determined to be $(0.55\pm0.2)\Delta E_g$ and was used in the EFA calculations of electronic and optical properties of the $PbTe/Pb_{1-x}Eu_xTe$ MQW's.

Two approaches are described for the analysis of transmission and reflectivity spectra multilayered semiconductor structures. The EFA-SL model calculation, which is based on a consistent envelope function approximation, yields transmission and reflectivity data in good agreement with the experimental data *without using any adjustable parameters* once the band offset is fixed. The EFA model yields the SL band structure not only at $\mathbf{k}=0$ but also at finite **k** (k_x,k_y,K) values. The optical constants are obtained from the knowledge of the electronic properties at finite **k** values, and $\alpha(\omega)$ is obtained from a numerical **k** integration over interband transitions using the envelope wave functions which are normalized to the superlattice period D. Thus the electronic interband contributions to the imaginary part of the dielectric function are not separated into contributions originating from transitions within either the well or the barrier layers. According to these calculations, $n(\omega)$ exhibits cusplike enhancements close to the interband transition energies between electric subband.

ACKNOWLEDGMENTS

We thank H. Krenn, C. Weisbuch, and M. Helm for helpful discussions. This work was supported by Fonds zur Förderung der Wissenschaftlichen Forschung, Vienna Austria, Project No. P8446.PHY.

[1]D. L. Partin, IEEE J. Quantum Electron. **QE-24**, 1716 (1988).

[2]Z. Feit, D. Kostyk, R. J. Woods, and P. Mak, Appl. Phys. Lett. **58**, 343 (1991).

[3]A. Ishida, S. Matsuura, M. Mizuno, and H. Fujiyasu, Appl. Phys. Lett. **51**, 478 (1987).

[4]W. Goltsos, J. Nakahara, A. V. Nurmikko, and D. L. Partin, Surf. Sci. **174**, 288 (1986).

[5]E. T. Heyen, M. Hagerott, A. V. Nurmikko, and D. L. Partin,

Appl. Phys. Lett. **54**, 653 (1989).
[6]L. S. Kim, H. D. Drew, R. E. Doezema, J. P. Heremans, and D. L. Partin, Phys. Rev. B **35**, 2521 (1989).
[7]M. Kriechbaum, P. Kocevar, H. Pasdiev, and G. Bauer, IEEE J. Quantum Electron. **QE-24**, 1727 (1988).
[8]F. Stern, Phys. Rev. **133**, A1653 (1964).
[9]J. N. Zemel, J. D. Jensen, and R. B. Schoolar Phys. Rev. **140**, A330 (1965).
[10]S. Yuan, H. Krenn, G. Springholz, and G. Bauer, Phys. Rev. B **47**, 7213 (1993).
[11]Y. Suzuki and H. Okamoto, J. Electron. Mater. **12**, 397 (1983).
[12]C. Weisbuch and B. Vinter, *Quantum Semiconductor Structures* (Academic, San Diego, 1991), p. 70.
[13]K. B. Kahn and J. Leburton, Appl. Phys. Lett. **47**, 508 (1985).
[14]S. Schmitt-Rink, D. S. Chemla, and D. A. B. Miller, Adv. Phys. **38**, 89 (1989).
[15]K. Nakamura, A. Shimizu, K. Fujii, M. Koshiba, and K. Hayata, IEEE J. Quantum Electron. **QE-28**, 1670 (1992).
[16]G. Springholz, G. Bauer, and G. Ihninger, J. Cryst. Growth **127**, 302 (1993).
[17]G. Springholz and G. Bauer, Appl. Phys. Lett. **60**, 1600 (1992).
[18]G. Bastard, *Wave Mechanics Applied to Semiconductor Heterostructures* (Editions de Physique, Paris, 1989), p. 13.
[19]H. S. Cho and P. R. Prucnal, Phys. Rev. B **39**, 11 150 (1989).
[20]S. Yuan, H. Krenn, G. Springholz, G. Bauer, and H. Kriechbaum, Appl. Phys. Lett. **62**, 885 (1993).
[21]W. Okulski and M. Zaluzny, Thin Solid Films **204**, 239 (1991).
[22]N. J. Johnson, H. Ehrenreich, P. M. Hui, and P. M. Young, Phys. Rev. B **41**, 3655 (1990).
[23]A. F. Terzis, X. C. Liu, A. Petrou, B. D. McCombe, M. Dutta, H. Shen, Doran D. Smith, M. W. Cole, M. Taysing-Lara, and P. G. Newman, J. Appl. Phys. **67**, 2501 (1990).
[24]B. Harbecke, Appl. Phys. **B39**, 165 (1986).
[25]M. Kriechbaum, in *Two Dimensional Systems: Physics and Applications,* edited by G. Bauer, F. Kuchar, and H. Heinrich, Springer Series in Solid State Sciences Vol. 63 (Springer, Berlin, 1984), p. 120.
[26]K. Böhner, *Spline Functions* (Teubner, Stuttgart, 1974).
[27]G. Karczewski, J. K. Furdyna, D. L. Partin, C. N. Thrush, and J. P. Heremans, Phys. Rev. B **46**, 13 331 (1992).
[28]G. Bauer and H. Krenn, in *Handbook of Optical Constants,* edited by E. D. Palik (Academic, Orlando, 1985), p. 535.
[29]G. Bauer, H. Pascher, and W. Zawadzki, Semicond. Sci. Tech. **7**, 703 (1992).
[30]S. W. Corzine, R. H. Yan, and L. A. Coldren, in *Quantum Well Lasers,* edited by P. S. Zory (Academic, Boston, 1993), p. 26.
[31]G. Lehmann and M. Taut, Phys. Status Solidi B **54**, 469 (1972).